JPRS-CST-93-008
28 April 1993

JPRS Report

Science &
Technology

China

19980115 032

Science & Technology
China

CONTENTS

SCIENCE & TECHNOLOGY POLICY

ADVANCED MATERIALS

LASERS, SENSORS, OPTICS

MICROELECTRONICS

TELECOMMUNICATIONS R&D

Nation's Software IPR Protection Highlighted

*93P60214A Beijing JISUANJI SHIJIE [CHINA
COMPUTERWORLD] in Chinese No 11, 24 Mar 93
pp 1-2*

[Article by Wu Hongqiao [0702 4767 2890]: "Software
Protection Stressed in Legislation: Nation's Software
Intellectual Property Rights Protection Progressing Rap-
idly"]

[Summary] Since China promulgated the "Copyright
Law" and "Computer Software Protection Regulations,"
worldwide computer circles have had great expectations
for this nation's software intellectual property rights
(IPR) protection. In a very short number of years,
China's software IPR protection has already embarked
on the path of international legislative protection. Many
foreign makers' software products have begun to enter
the Chinese market, and at the same time the legal
system for domestic software circulation and exchange is
undergoing a process of strengthening and perfecting. All
of this activity has opened up channels for the entry of
domestically made software into the international soft-
ware market.

China's efforts to establish and promote software IPR
protection can be seen in the following list of major
events:

In September 1990, China promulgated the "Copyright
Law," including computer software as an example of
works protected by copyright.

In June 1991, China promulgated the "Computer Soft-
ware Protection Regulations."

In May 1992, the nation promulgated the "Computer
Software Copyright Registration Measures" and for-
mally began to implement protection regulations.

In September 1992, the State Council promulgated the
"Stipulations for Implementing the International Copy-
right Treaty."

In October 1992, China entered the "Bern Convention
for the Protection of Literary and Artistic Works" and
the "World Copyright Convention."

On 20-23 October 1992, the Ministry of Machine-
Building and Electronics Industry (MMEI) Computer
Department and IBM China jointly held a "Sino-U.S.
Computer Software IPR Symposium" to promote the
execution of China's software protection rules and regu-
lations, to provide tutorials, and to permit interchange of
experiences and development trends in international
software protection, as well as to promote understanding
and cooperation between Chinese and foreign IPR cir-
cles.

On 30 October 1992, a major move critically impacting
IPR protection occurred: the China National Electronics
Import and Export Corporation along with several
domestic computer production plants represented by

China Great Wall (GW) Computer Group reached agree-
ment in Beijing with the U.S. firm Microsoft Corp. on
the authorized use of MS-DOS5.0. This is the first
large-scale usage agreement signed by Chinese computer
manufacturers and a major foreign software firm.

In December 1992, the nation's first software copyright-
infringement case was brought—Beijing Weihong [1792
1347] Computer Software Institute accused the Chinese
Academy of Sciences (CAS) Yuanwang [6678 2598]
Technology Company via its Heima ["Black Horse"]
Software Sales Division of illegally deciphering and
selling the "UNFOX2.1 Reverse Compiler Doctor" soft-
ware developed by the institute; the case was accepted
and heard in the Beijing Municipality Haidian District
People's Court. "UNFOX2.1 Reverse Compiler Doctor"
was one of the first 10 domestic software products
receiving computer software copyright registration cer-
tificates on 15 June 1992 [see article in 8 July 1992 issue
of this newspaper (summarized in JPRS-CST-92-016, 20
Aug 92 p 16)]. This case was decided a few days ago, with
the plaintiff winning the lawsuit: Weihong was awarded
damages of 46,000 yuan.

Also in December 1992, a U.S. commercial software
alliance held a "Software Protection Exchange Forum"
in the Beijing New Century Hotel. Public figures at this
forum expressed confidence that Chinese government
officials as far as possible would protect the rights of
copyrighters and as quickly as possible would improve
current software protection rules and regulations. Simul-
taneously, the alliance announced the 1993 launch in
China of a vigorous [structured] activity for software
protection popularization; this activity would include
representatives from government, industry, and major
software users groups and would involve organizing
symposia in Beijing, Shanghai, and other places.

Physics Issues in Arms Control

*93FE0475A Beijing WULI [PHYSICS] in Chinese
Vol 21 No 11, Nov 92 pp 654-659*

[Article by Du Xiangwan [2629 4382 3834] and Li Bin
[2621 1755] of Beijing Institute of Applied Physics and
Computational Mathematics, Beijing 100008, Song
Jiashu [1345 1367 2885] of the Chinese Nuclear Mate-
rials Society, Beijing 100082, and Zhu Guangya [2612
0342 0068] of the Chinese Society of Science and Tech-
nology, Beijing 100081: "Physics Issues in Arms Con-
trol"]

[Text] **Abstract**

There are many scientific and technological problems in
arms control research—such as weapons capability and
war effect, systems analysis of arms control, verification
techniques, and weapons destruction techniques—that
involve a wide variety of physical problems. This study
is gradually evolving into a new branch of applied
physics which may be called "arms control physics." Its
development not only gives an impetus to the course of

disarmament and world peace but also enriches the contents of modern physics.

In the past several centuries, battlefield weapons turned from cold to hot. Today, there are conventional, biological, chemical and nuclear weapons in the stockpile, and even the possibility of space weapons. The superpowers spent a great deal of manpower and resources to compete in the weapons race that threatens the existence of mankind. Under the circumstances, arms control is critical to the conservation of resources and the minimization of the threat of world war and its associated losses.

Arms control is designed to limit the deployment, stockpiling, production and testing of certain weapons and to implement a number of measures to control the arms race and to provide safety and protection. Therefore, arms control is more general in concept than disarmament. Initially, arms control research was carried out in the domain of social science such as politics, law and diplomacy. Since 1980, arms control has gradually entered an implementation phase and has begun to involve more problems in the natural science domain. Nuclear and space weapons are major issues in arms control today, and mostly involve problems associated with physics. Thus, arms control physics becomes a new branch of science. Presently, arms control physics is becoming a new branch of applied physics. The scope of research includes various physical and technological problems associated with arms control, such as weapons capability and war effect, systems analysis of arms control, verification techniques, and weapons production and destruction techniques, etc.

I. Weapons Capability and War Effects

Assessment of the capability of a weapon includes the study of its destructive mechanism, destructive power, survival capability and cost. These issues are important not only to weapons experts but also in arms control research. Weapons experts and arms control scientists may have differences of opinion on the destructive power and survivability of weapons. For example, after President Reagan presented the SDI (Strategic Defense Initiative) in 1983, the American Physical Society (APS) and the Strategic Defense Initiative Office (SDIO) held different views in the assessment of directed energy weapons.[1]

First, the capability of a certain weapon is the basis of studying arms control by means of systems analysis. For instance, if one wants to calculate the total destructive power of the nuclear weapons owned by a certain country, one cannot simply count the number of nuclear weapons that country has because different models may correspond to substantial differences in their TNT equivalents. However, it is not a simple addition of the equivalent weights. Instead, one must add up the "effective equivalent megatons." "Effective equivalent megatons" is the $2/3$ power of the TNT equivalent weight (in units of million tons). The reason for this definition is

that research on nuclear arms effects shows that the area of destruction of a nuclear weapon on the ground is proportional to the 2/3th power of its TNT equivalent. When a combat model is established (see next section), it is necessary to know the SSKP (single-shot kill power) for each warhead of all the intercontinental ballistic missiles (ICBMs). This quantity is also a function of the effective megaton equivalent.

Next, the study of arms capabilities itself has some significance with regard to arms control. In principle, the existence of a spear causes the invention of a shield; the ultimate weapon does not exist. The presence of a new weapon often causes a new arms race. Therefore, a detailed study of the effects of weapons may let the decision maker realize that the development of this new weapon does not have much significance because of the presence of certain countermeasures. In addition, during the early stages of development, the new weapon itself is often mythicized and beautified. Scientific proof can unveil the true effects and capabilities of these new weapons. One of the reasons for the signing of SALT I between the United States and the former USSR is that scientists proved that it would be extremely difficult to intercept an ICBM based on technology existing then. Furthermore, it would be too costly to make the "effect-to-cost ratio" attractive.

In 1983, the U.S. government proposed the SDI concept and claimed it to be a purely defensive weapons system. By studying the destruction mechanism and kill power of SDI, scientists from different countries proved that the anti-missile capability of the SDI can be used to attack satellites.[2] This kind of weapon is not a purely defensive system such as a gas mask. This viewpoint is being widely accepted and plays an important role in curbing the arms race in space.

The effect produced by a number of weapons at the same time may not be limited to the summation of the effects from individual weapons. A compound effect may result, i.e., a war effect. Presently, the effect of nuclear war has been studied in detail and depth. In a large-scale nuclear war, hundreds, or even thousands, of nuclear warheads explode within a very short period of time. In addition to the kill and destructive power caused by the intense shock wave, light irradiation, early-stage nuclear radiation, radioactive contamination and nuclear electromagnetic pulse, there are some other compound effects. The two major compound effects[3,4] are falling ground temperature and thinning of the ozone layer.

In 1983, Turco et al.[4] presented the nuclear winter theory. In a large-scale nuclear war, fire will sweep across a large number of industrial centers, cities and forests. The smoke particles produced are relatively small and can float in the atmosphere for long periods of time. In time, the smoke and the dust sucked up by nuclear explosions will permeate over most of the earth's surface to reduce the amount of sunlight reaching the surface. This will cause the ground temperature to drop, which will result in cold weather and famine. In order to

estimate the magnitude of temperature drop, Turco et al. established a nuclear war model, a particle-microscopic physics model and a radiation-convection model. Later on, other scientists conducted similar studies and reached the same conclusion that a substantial drop of ground temperature will occur. However, the magnitude of the temperature fall varied from study to study.

The center of the fireball produced by a nuclear explosion reaches several million degrees in temperature. Nitrogen monoxide is formed by nitrogen and oxygen near the fireball. It rises with the fireball to the upper atmosphere and there it reacts with ozone to form nitrogen dioxide. Ozone is consumed in large quantities to thin out the ozone layer. Therefore, the amount of ultraviolet light penetrating the atmosphere increases significantly. This process starts before nuclear winter and continues for some time after nuclear winter ends. Intense ultraviolet light will result in severe burns to humans, animals and crops, making the living environment extremely harsh.

The study of war effects by physicists made people realize that even when the opponent is stripped of nuclear retaliation capability after launching a large-scale nuclear attack, the aggressor will also have to face the tremendous disaster brought about by the effects of a global nuclear war. This makes countries with nuclear capability maintain an extremely cautious attitude toward nuclear war.

II. Systems Analysis for Arms Control

Physicists introduced a number of quantitative analysis concepts and techniques in arms control research. They became the language accepted by scientists, and even diplomats. For example, in nuclear arms control research, crisis stability and arms race stability are two extremely important concepts. The former represents the probability of not launching the first strike by either of the two opposing sides during a crisis. The latter represents the intensity of the incentive for arms race. These two concepts have been clearly defined mathematically[5] and are widely used to assess various arms developments and disarmament plans. These definitions are still too rough from the viewpoint of physicists. However, they are a giant step forward compared to pure descriptive research.

With the above definitions, systems analysis techniques can be employed to determine whether a disarmament plan meets the welfare of a certain country and enhances world peace as well, how the introduction of a new class of weapons would escalate arms race, and whether a disarmament plan can be effectively implemented.

A war model must be established first. A war model has been used to describe the combat process for conventional weapons. The following discussion is limited to a strategic war model. The characteristics and numbers of weapons and targets on both sides are considered as elements in the system under investigation and they are mutually dependent. The dependency can be determined

based on the capability of the weapons and the characteristics of the targets and expressed in mathematical form. In nuclear warfare, the relation between the number of attacking warheads and the number of underground silos destroyed can be determined based on SSKP. The quantity of weapons developed during the same era can be computed from the cost of each weapon and the total military expenditure. A model can be established with the information discussed above to describe the strategic combat process, i.e., the consumption and loss of strategic weapons during the war. Since strategic weapons are not significantly impacted by the environment and are relatively limited in quantity, the war model is much more reliable than that developed for conventional weapons. Different outcomes can be obtained by inputting different quantities of weapons and specifications. Therefore, it is possible to determine which factors are helping or hurting crisis stability and arms race stability.

Sagdeev[6] did an analysis on START and concluded that this kind of disarmament would not lower crisis stability. Kerby studied the impact of SDI on crisis stability and concluded that the deployment of SDI by one side or both sides would harm crisis stability.

It is also possible to analyze the development trend of the arms race using war model results in order to assess arms race stability. If one side is developing a new weapon, the strength of the other side is consequently weakened. Hence, the latter will develop a suitable weapons system to counter the new weapon's effect. With given economic and technological constraints, it is possible to calculate the arms development situation during the race on the basis of the war model and a given model of arms development. Some preliminary results[7] indicate that SDI will not shift the direction of arms development toward defense. Instead, it will lead to arms race instability.

Another application of systems analysis in arms control research is to demonstrate the reliability of disarmament treaties. There are three factors influencing a country to violate a treaty; i.e., how much benefit can it receive from treaty violation, how strongly can the treaty be verified, and how strong a reaction would treaty violation produce. For instance, one can demonstrate what kind of seismic verification network is required to ensure the implementation of the "Equivalent Limitation Treaty" based on these three factors.

III. Verification Techniques

A key point in arms control physics is verification techniques. It plays a critical role in the implementation of treaties. Therefore, different national governments and the United Nations are concerned about verification.

1. Verification of Nuclear Testing[8]

In order to monitor the implementation of the "Equivalent Limitation Treaty" and to reach an accord on the

"Nuclear Test Ban Treaty," underground nuclear explosions must be verified. There are two main verification methods, i.e., seismic and fluid dynamics. Natural seismic activity is caused by movement of rock strata. It is large in scale and lasts a long period of time. Hence, the seismic wave produced is primarily a transverse wave and it is mainly in the low-frequency band. The duration of a nuclear explosion is short and the seismic wave produced is from high-pressure compression of rocks. Therefore, the accompanying seismic wave is a high-frequency longitudinal wave. Based on these differences, it is possible to distinguish an earthquake from a nuclear explosion. The maximum amplitude of the seismic wave at a certain location is a function of the equivalent weight of the device. By measuring the Richter scale of the seismic wave, it is possible to estimate the equivalent weight of the device by using an empirical equation. The UN Disarmament Commission has a group of experts investigating this technique. They are primarily staffed with seismologists and physicists.

After an underground explosion is set off, a shock wave begins to propagate outward at a very high speed. At the beginning, the wavefront velocity of the shock wave is a function of the equivalent weight of the device. This relation can be calculated using fluid dynamics. Scientists have developed a continuous reflection measurement to determine radius as a function of time, i.e., the CORRTEX technique, to determine the wavefront velocity of the shock wave.[8] The fluid dynamics method provides a more accurate estimate of the equivalent weight than the seismic method. There are more accurate techniques for the side that conducts the test to estimate the equivalent weight of the device. However, these methods are considered too invasive for verification and are not considered acceptable techniques.

2. Verification of Nuclear Warheads

In a disarmament process (such as START), many warheads are removed from their deployment sites. In order to ensure that the number of warheads is indeed reduced, one needs verification. Verification of nuclear warheads can be done either actively or passively. The active method is to generate an external signal for detection by excitation. For instance, neutrons may be used to excite fissionable materials in a warhead in order to detect neutrons and γ rays released by fission. The passive method is to observe signals emitted by the material itself, such as detecting neutrons and γ rays released by spontaneous fission. Much theoretical work has been done in this field.[9] With the support of the former USSR government and military, U.S. and USSR scientists conducted large-scale tests to prove the verifiability of nuclear warheads.[10]

3. Verification of Plutonium Production for Military Use in Non-Proliferation of Nuclear Arms Treaty

U-238 can be converted to Pu-239 by neutron irradiation in a reactor. If the duration of irradiation is lengthened, Pu-240, or even Pu-241, may be produced. Pu-239 may be used to build nuclear weapons. However, plutonium containing Pu-240 and Pu-241 isotopes is not suitable for making atomic bombs because of its low efficiency. The reason is that Pu-240 has a very high spontaneous fission rate. Chain reaction takes place before full compression is completed, thus lowering the fission power of the device.[11] Therefore, reactors are required to maintain a long fuel-usage cycle so that sufficient Pu-240 and Pu-241 are produced. Thus, no weapons-grade plutonium can be produced by the reactor. The refueling cycle of a reactor can be monitored by placing seals or installing monitors.

4. Verification of Laser Weapons Testing[12,13]

Ground-based high power lasers are a class of important anti-missile weapons in the SDI. In order to develop ground-based anti-missile lasers, tests must be done to study the transmission of high power lasers through the atmosphere. Laser light will be scattered by aerosol particles in the atmosphere. The intensity of scattered light is proportional to the power of the laser. On the other hand, the laser power reaching the target must be above a threshold level to deliver an effective kill power. Hence, scientists propose measuring scattered light intensity to monitor the laser power used in the experiment. This may provide a way to verify the limit of laser power to be used in experiments to be set in the future.

5. Verification of Space Reactors

The deployment of space weapons such as space-based directed energy weapons and electromagnetic rail guns may involve the use of reactors in space. Therefore, limiting space-based reactors may also limit a considerable number of space-based weapons.[14] When a reactor operates in space, because of its high temperature, it emits an intense infrared radiation. Based on reactor power, heat-dissipation mechanism, and resolution of existing infrared telescopes, Hafemeister[15] proved that operating space reactors can be effectively verified.

Space weapons—such as electromagnetic rail guns, particle-beam weapons and lasers—to be launched into outer space can also be verified according to their characteristics at satellite launch sites.[11]

To develop a verification technique for arms control, a theoretical model usually must be established to determine the characteristics of the subject of interest. Then, a verification technique is designed based on the resolution of existing detectors. Furthermore, the feasibility of the technique must be demonstrated. Verification techniques used in arms control must be effective; in other words, the method must be sensitive enough to avoid mistakes. In the meantime, the method must also be acceptable to the other party. This requires that the method is not too sensitive to gather excessive information. It would not be acceptable if military secrets are exposed as a result. Therefore, verification techniques must be sensitive to this point. This is the challenge in the research of verification techniques for arms control.

IV. Technology Associated With Arms Destruction

Upon the signing of disarmament treaties, disarmed weapons must be destroyed to ensure that these weapons will not be redeployed. Starting from the verification and confirmation of weapons to be disarmed to rendering the weapons useless or too costly to restore, the entire process involves a variety of complex technologies. Not only is it necessary to ensure that the weapons to be disarmed are destroyed, one also needs to make sure that no military secrets are leaked and the storage of dismantled weapons will not pose any threat to mankind in the years to come. First, one must ensure that weapons verified to be disarmed are not switched in the dismantling process. A "fingerprint" labeling technique may be employed. A "fingerprint" is a recognizable signature of an individual weapon that cannot be altered easily. For example, the neutrons and γ rays generated from spontaneous fission in the warhead are absorbed upon penetration of the case and emit new γ rays. Since the structure, composition and manufacturing date of each warhead are different for each warhead, the γ-ray energy spectrum measured outside the warhead is also slightly different. The γ-ray energy spectrum for each warhead is measured at a fixed location and stored as its "fingerprint" to prevent any switching of warheads. This labeling technique applies a unique marker that cannot be easily duplicated on the weapon after verification. Some have proposed adding fine crystals in a coating to be applied on the weapon; then, a photograph is taken by shining light at a fixed angle for verification. The crystal distribution and orientation is completely random; it is almost impossible to create two identical patterns. Labeling and "fingerprinting" can also be considered as a part of verification.

Labeled or fingerprinted weapons are packed and shipped to the factory for disposal. Different components are destroyed in different shops. Let us use the destruction of nuclear warheads as an example.[16] The label or fingerprint of each nuclear warhead must be reverified upon arrival at the factory prior to disposal. The tritium recovered from the warhead will be returned to the owner of the warhead to replenish the tritium loss due to decay (half-life 12 years) in warheads not slated to be disarmed. High explosives are to be combusted in a special shop. Other non-nuclear components are crushed. The processing of fissionable materials is more complicated. Since the kill power of the warhead is closely related to the composition and amount of fissionable materials it contains, in order to keep this information confidential, fissionable materials from different models of warheads are mixed prior to processing. Concentrated uranium is diluted with natural uranium and then used as reactor fuel. Pu-239 is mixed with reactor waste and then put in storage. As discussed earlier, this kind of plutonium can no longer be used to make nuclear weapons.

It is costly and time consuming to dilute fissionable materials. Therefore, direct storage of undiluted fissionable materials should be considered. However, one must

prevent them from reaching a critical state. Rigid and stable materials may be used to isolate subcritical fissionable materials. The distance of separation can be calculated based on the hardness of the separator and the possible compression strength.

Controlling the production of weapons and relevant materials can ensure that dismantled weapons do not get replaced. Furthermore, control of production of materials may lead to the destruction of weapons already in place. For example, some have suggested that nuclear warheads be naturally reduced through a ban on the production of tritium. Some nuclear warheads require tritium; however, 5 percent of tritium is lost per year by natural decay. If tritium is not replenished, 5 percent of the warheads will become obsolete.

Not all technical issues related to the destruction of weapons involve physics. Other fields in natural science are also required. Presently, the study of weapons destruction is far behind that of verification. The fundamental reason is that verification has been an ongoing effort for many years, while weapons destruction just began recently. The disposal of fissionable materials is still in a discussion phase. Real disarmament must include destruction of weapons. Therefore, destruction of weapons will attract a great deal of attention in the near future.

Arms control physics is an applied science that involves many fields in physics, including nuclear physics, engineering physics and laser physics. In addition, it is an interdisciplinary subject that is closely related to international politics, international law, economics and engineering. Research done by physicists on arms control has helped people understand the harm of arms races and nuclear war to mankind. Arms control research is also made scientific and quantitative by physicists. Furthermore, effective verification and destruction techniques have been made available for arms control. The creation and development of arms control physics provides an impetus to the advancement of arms control research as a whole. It plays an important role in promoting disarmament and world peace. In addition, it also enriches the content of modern physics.

Currently, there are many physicists engaged in arms control physics research. A number of research organizations have been established, such as the Arms Control Society, the Association of American Scientists, and the Committee of Scientists of the former USSR. China also has research scientist groups. These groups have made a substantial contribution to the advancement of arms control physics and academic exchange in this area. Presently, besides some unscheduled meetings, there is the famous annual Pugwash Conference and the Summer Course in Science and World Affairs. In 1991, the Pugwash Conference was held in Beijing. The 1992 Summer Course in Science and World Affairs was also held in China. Major accomplishments in arms control physics research are primarily published in the form of a symposium or a special book. However, some have been

recently published in physics journals. For instance, PHYSICS TODAY has a special column on arms control. The presence of a professional journal, SCIENCE AND GLOBAL SECURITY, signifies that research on arms control physics has entered a new era.

References

1. Report to the American Physics Society of the Study Group on Science and Technology of Directed Energy Weapons, 1987.

2. Du Xiangwan et al., "Stop Weapons in Space—An Urgent Task in Arms Control," China Institute of Nuclear Information, 1990, CNIC-00401.

3. D. Schroeer, "Science, Technology, and the Nuclear Arms Race," John Wiley & Sons, New York, 1984, p 95.

4. R. P. Turco et al., SCIENCE, Vol 222, 1983, p 1283.

5. P. L. Chrzanowski, Energy and Technology Review, Uni. of California, 1987, UCRL-52000-87-1-2.

6. R. Z. Sagdeev and A. A. Kokoshin, "Selected Readings in Arms Control & Disarmament," Vol 9, 1990, p 12.

7. A. M. Saperstein and G. Mayer-Kress, J. OF CONFLICT RESOLUTION, Vol 32, No 4, 1988, p 638.

8. Report of the OTA on Seismic Verification of Nuclear Testing Treaties, 1988, 050888, OTA.

9. S. Fetter et al., SCIENCE AND GLOBAL SECURITY, No 1, 1990, p 225.

10. S. Fetter et al., SCIENCE AND GLOBAL SECURITY, No 1, 1990, p 323.

11. Same as reference 3, p 287.

12. T. H. Braid, SCIENCE AND GLOBAL SECURITY, No 2, 1990, p 59.

13. A Study Group Report on the Federation of American Scientists, Laser Asat Verification, 1991.

14. Du Xiangwan et al., XLI-C15, 41st Pugwash Conference on Science and World Affairs, 17-22 September 1991, Beijing, China.

15. D. W. Hafemeister, SCIENCE AND GLOBAL SECURITY, No 1, 1989, p 73.

16. T. B. Taylor, SCIENCE AND GLOBAL SECURITY, No 1, 1989, p 1.

Microstructure of Rapid Solidified TiAl Alloy Powder

[Article by Cao Mingzhou [2580 0682 3166], Han Dong [7281 2639], Zhang Tao [1728 3347], and Li Dong [2621 2639] of the Institute of Metals Research, Chinese Academy of Sciences, Shenyang: "Microstructure of Rapid Solidified TiAl Base Crystallites"; MS received 15 Jan 92, revised 25 May 92]

[Text] Abstract: Crystallite alloy powders with the composition Ti-34Al-2Mn were made by gas atomization method. The typical size of the rapid solidification (RS) powders is 27 μm. X-ray diffraction data show that the RS powder mainly consists of α_2-phase with minor amount of γ-phase. The microstructure of RS powders displays equiaxed grains and dendritic grains. After the 900°C, 2 h vacuum annealing, most α_2-phase transforms to γ-phase, and the grain size becomes finer.

The intermetallic compound TiAl has attractive combined properties such as high modulus of elasticity, high temperature strength, good creep property, low density, etc. It is a new aircraft structural material with potential. However, the compound is brittle at room temperature, which limits its application. In the past, an alloying method was used to improve the drawbacks of the TiAl alloy.[1] Recently it has been discovered that the rapid solidification (RS) method can greatly refine the alloy's structure, and could probably improve the room-temperature brittleness of the TiAl alloy.[2] This article studies the microstructure of the TiAl-Mn alloy crystallites made by the RS method.

1. Experimental Methods

A TiAl-Mn alloy ingot with the chemical composition (wt-%) of Al-33.8, Mn-2.02, O-0.18, H-0.029 and Ti-balance was made by melting and casting. The ingot was then melted and gas atomized into crystallite powders. The particle size distribution, as shown in Figure 1, was determined by the sedimentation method; typical particle size is 27 μm. The surfaces of the powders were etched by diluted Kroll solution and observed for solidified surface under a scanning electron microscope (SEM). A portion of the powder was annealed at 900°C for 2 hours (h) in vacuum. An optical microscope was used to study the powder microstructure. An X-ray diffractometer was used to analyze the phase composition, and the space lattice parameters.

2. Experimental Results and Discussion

The particle shape of the RS Ti-34Al-2Mn powder is spherical as shown in Figure 2a [photograph not reproduced]. After etching, the spherical surface displays equiaxed grains, as shown in Figure 2b. Figure 3 [photograph not reproduced] shows the microstructure of the
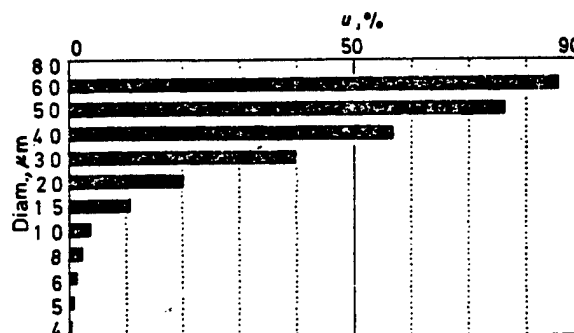

Figure 1. Size Distribution of RS Powder of Ti-34Al-2Mn Alloy

powder cross sections. The smaller spheres display equiaxed grains. The larger spheres contain two different zones: in the outer zone, the grains are essentially equiaxed; and in the inner zone, the grains are dendritic. From the morphology of the RS titanium powders, the cooling rate can be calculated according to the following equation:[3]

$$\lambda = B(\varepsilon)^{-n}$$

where λ is the size of the equiaxed grains or the distance between two dendrites, ε is the cooling rate, and B and n are constants. For the equiaxed grain structure: $B = 3 \times 10^4$ μm $(K/s)^n$, where $n = 0.62$; and for the dendritic structure: $B = 45$ μm $(K/s)^n$, where $n = 0.31$. Based on the structure as shown in Figure 3, we can estimate that the cooling rate for the equiaxed grain structure is approximately 1.8×10^6 K/s, and that for the dendritic structure, 2×10^5 K/s. It is obvious that for a larger grain, the cooling rate of the core is lower than that of the surface.

The microstructures of the powders also show that some of the powders are fractured. After the 900°C, 2 h vacuum annealing, the fractured powder particles practically disappear. Due to the fact that the microstructures of the fractured spots are continuous, it is quite possible that the fractures were caused by the internal stress induced by the rapid cooling combined with the cutting action of grinding during sample preparation.

The X-ray diffraction shows that the RS powder displays a pattern of strong α_2-phase (DO_{19}) peaks mixed with weak γ-phase (Ll_0) peaks as shown in Figure 4. According to a recently published Ti-Al phase diagram,[4] the solidification of the Ti-34Al-2Mn alloy first goes through the α-phase zone, and further cooling will transform the γ-phase to the $\alpha_2 + \gamma$ phase. The high speed cooling will shift the α_2-phase composition toward the Al rich direction.[5] By so doing, the RS Ti-34Al-2Mn alloy powder consists of mainly the α_2-phase mixed with a minor amount of the γ-phase.

After the 900°C, 2 h vacuum annealing, the powder does not show any surface change under the SEM observation. However, significant changes (Figure 5 [photograph not
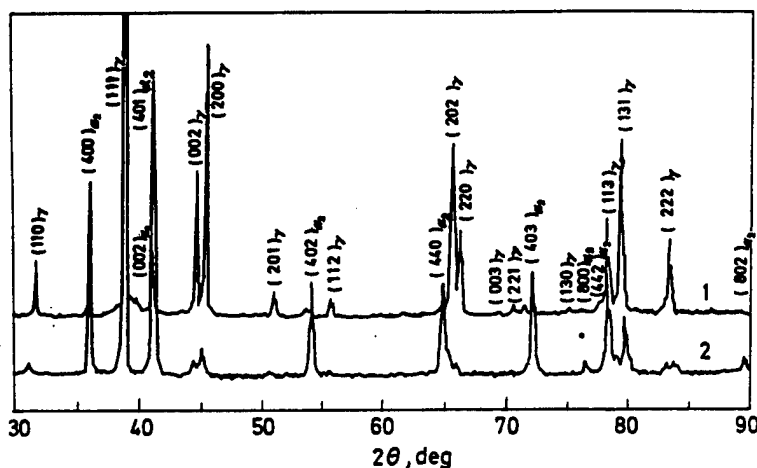
Figure 4. X-Ray Diffraction Spectra of Ti-34Al-2Mn Alloy Powder, CuK$_\alpha$

1. as RS produced; 2. annealed at 900°C, 2 h in vacuum

reproduced]) occur in the powder morphology under the optical microscope observation. The powder microstructure transforms to very fine equiaxed grains. The fact that the γ-phase becomes strong in the X-ray diffraction pattern and the α$_2$-phase becomes comparatively weak as shown in Figure 4 indicates that the transformation of α$_2$ → γ occurs. The γ-phase segregation from the α$_2$-phase is the main reason for the grain refining.

The lattice parameters of the α$_2$-phase and the γ-phase in the two different powder conditions are determined as shown in Table 1. We can see that the 900°C, 2 h vacuum-annealed sample shows that both the a and c axes of α$_2$ increase and c/a also increases slightly; the a axis of γ-phase decreases but the c axis increases and c/a

also increases. Reference 5 indicates that in the Ti-Al binary alloy system, both the a and c axes of the α$_2$-phase increase with the decrease of Al content. In the γ-phase, the a axis decreases and the c axis increases with increase of Al content. Therefore, Table 1 shows clearly that the α$_2$-phase in the RS Ti-34Al-2Mn crystallites is metastable, because its Al content is higher than that in the equilibrium condition. After vacuum annealing, the segregated γ-phase decreases the Al content in the metastable α$_2$-phase. At the same time the Al content in the γ-phase continuously increases. The experimental data shows that the lattice parameters of the α$_2$-phase of the 900°C, 2 h vacuum-annealed powder are very close to the parameters of the Ti$_3$Al binary alloy in the as-cast condition (a = 0.576 nm, c = 0.465 nm, c/a = 0.808).

Table 1. The Lattice Parameters of α$_2$ and γ-Phase in Ti-34Al-2Mn Alloy Powder

State	α$_2$-phase			γ-phase		
	a (nm)	c (nm)	c/a	a (nm)	c (nm)	c/a
Rapid cooling	0.5740	0.4613	0.8037	0.4003	0.4058	1.0137
900°C, 2 h in vacuum	0.5781	0.4674	0.8085	0.3998	0.4067	1.0173

3. Conclusions

(1) The typical particle size of the ultrasonic-gas-atomized Ti-34Al-2Mn alloy crystallite powder is 27 μm. The cooling rate is 10^5-10^6 K/s.

(2) The microstructure of the RS powder consists of the α$_2$-phase with a minor amount of the γ-phase.

(3) After the 900°C, 2 h vacuum annealing, the α$_2$ → γ transformation disintegrates the block α$_2$-phase and further refines the structure.

References

1. Hashimoto, K., Doi, H., Kasaha, K., Nakano, O., Tsujimoto, T., Suzuki, A., PROCEEDINGS OF THE JAPAN INSTITUTE OF METALS, 1988; 52: 1159 (in Japanese).

2. Teal, K. R., Eylon, D., Froes, F. H., In: Lacombe, P., Tricot, R., Beranger, G., eds., 6th World Conf. on Titanium, Les Ulis Cedex, Les Editions de Physique, France, 1988: 1121.

3. Baeslock, W. A., Weeter, L., Krishnamurthy, S., Smith, P., In: Kear, B. H., Giessen, B. C., eds., Mater. Res. Soc. Symp. Proc., Vol. 28: Rapidly Solidified Metastable Materials, 1984: 375.

4. Hall, E. L., Huang Shih-Chin, ACTA METALL. MATER., 1990; 38: 539.

5. Han Dong, Cao Mingzhou, Li Dong, Proceedings of 7th National Conference on Titanium Alloys, Guangzhou, 1990: 389.

6. Ence, E., Margolin, H., TRANS. AIME, 1961; 221: 151.

Improvement in Tensile Properties of α + β Type Ti Alloys by Hydrogen Treatment

[Article by Gong Bo [1362 3134] and Lai Zuhan [6351 4371 3211] of Northeast University of Technology, Shenyang, Niinomi Mitsuo and Kobayashi Toshiro of Toyohashi University of Technology, Japan: "Tensile Properties of α + β Ti Alloys Improved by Hydrogen Treatment," funded by the Natural Science Foundation of China; MS received 4 Mar 92, revised 30 Jun 92]

[Text] Abstract: A process to refine the microstructure of α + β titanium alloy by hydrogen is developed. The alloy is hydrogenated 0-40K below the hydrogenized-β transition point, cooled to room temperature, and then de-hydrogenated at 948K in vacuum. The microstructures of the Ti-6Al-4V and Ti-5Al-2.5Fe alloys are refined after the treatment. Their yield stress, tensile strength, and elongation are improved by 8-15 percent, 5-13 percent, and 7-14 percent respectively.

1. Experiment

The starting materials were annealed Ti-6Al-4V plates and non-annealed Ti-5Al-2.5Fe forgings. Their chemical compositions are as follows:

Alloy	Al	V	Fe	C	N	O	H
Ti-6Al-4V	5.96	4.09	0.15	0.01	0.093	0.0034	0.005
Ti-5Al-2.5Fe	4.99	<0.01	2.37	0.01	0.016	0.100	0.0023

The test specimens were first made into blanks of 12 mm in diameter and 55 mm in length. The longitudinal axis of each blank was in parallel with the rolling direction. After hydrogen treatment, the blanks were made into tensile specimens of 4 mm in diameter and 20 mm in length.

Published papers used the following hydrogen treatment process: hydrogenating, β solid solution treatment, aging, and vacuum de-hydrogenating. The β solid solution treatment can be conducted either before,[1] or after,[2] or during[3,4] hydrogenating. The strengths of the hydrogen-treated samples increased apparently, but their plasticity suffered losses.[5] The significant feature of the newly developed hydrogen treatment process reported in this paper is as follows: the specimen is hydrogenated at a temperature below the hydrogenized β (H-β) transition point and then vacuum de-hydrogenated. The purpose is to avoid or to control the β-phase transformation to improve plasticity. The H-β transition point is the α/β transition point of the alloy during the hydrogenating treatment. The metallographic method has determined the H-β transition points for the Ti-6Al-4V and Ti-5Al-2.5Fe alloys to be 1063 and 1023K respectively. For comparison, the high-temperature hydrogen treatment process (hydrogenating above the H-β point)[3] was also used for this experiment. Hence, the hydrogenating temperatures for the Ti-6Al-4V specimens were 1023, 1053, and 1123K (high-temperature hydrogen treatment), respectively; and those for the Ti-5Al-2.5Fe specimens, 1003, 1023, and 1053K (high-temperature hydrogen treatment), respectively.

All specimens were hydrogenated in flowing high purity hydrogen for 2 h, and then cooled to room temperature. Weighing method was used to determine the hydrogen content of each specimen. The de-hydrogenating process was conducted by annealing the specimens at 948K for 8 h in vacuum. After de-hydrogenating, each specimen contained less than 0.002 wt-% of hydrogen.

Tensile test was conducted with a 10t Instron electronic tensile testing machine. The crosshead velocity was 0.5 mm/min.

2. Results and Discussion

Figure 1 and Figure 2 [photographs not reproduced] show the original microstructures of the Ti-6Al-4V and Ti-5Al-2.5Fe alloys and the microstructures after hydrogenation respectively. The original Ti-6Al-4V microstructure displays equiaxed (α + β) structure and the original Ti-5Al-2.5Fe microstructure displays coarse deformed (α + β) structure as shown in Figure 1a and Figure 2a, respectively. The hydrogen treatment apparently refined the structures of both alloys. After de-hydrogenating, the microstructures of the alloys hydrogenated above the H-β transition point display α-phase segregated along the grain boundaries of β grains as shown in Figure 1b. After de-hydrogenating, the microstructures of the alloys hydrogenated below the H-β transition point do not reveal any α network, as shown in Figure 1c and d. The microstructures of the alloys hydrogenated at the H-β transition point display partial grain boundary α-phase, as shown in Figure 2b.

Table 1 shows the mechanical properties of these alloys before and after the hydrogen treatment. The strengths and the plasticity of the alloys treated by the new process have apparently improved. The improvements of the Ti-6Al-4V alloy treated by the 1023K hydrogenating process are as follows: yield strength (YS) and the ultimate tensile strength (UTS) increased by 15 percent and 13 percent, respectively; and elongation (El) and reduction of area (RA), 7 percent and 56 percent, respectively. The improvements of the Ti-5Al-2.5Fe alloy treated by 1023K hydrogenating process are: YS and UTS increased by 8 percent and 5 percent, respectively; El and RA, 14 percent and 43 percent, respectively.

Improvement of the UTS of Ti-5Al-2.5Fe is lower because the starting material was in forged condition. Table 1 also shows the mechanical properties of the annealed Ti-5Al-2.5Fe alloy. Compared with its properties in the annealed condition, the hydrogen-treated Ti-5Al-2.5Fe improved approximately 11 percent, about the same as that of the Ti-6Al-4V. The alloys treated at high hydrogenating temperature have the same or slightly lower YS than those of the alloys treated by the new process. However, their elongations are 10-29 percent and 21-34 percent lower compared with the alloys in the original conditions and the alloys treated with the new process, respectively.

Table 1. Mechanical Properties of Ti-6Al-4V and Ti-5Al-2.5Fe Alloys

Alloy	Treatment	H_2 (wt-%)	0.2% YS (MPa)	UTS (MPa)	El (%)	R of A (%)
Ti-6Al-4V	As received	-	829	876	15.0	31.7
	1023K 2h+H_2	1.07	954	991	16.0	49.5
	1053K 2h+H_2	0.98	977	999	15.1	46.7
	1123K 2h+H_2	0.75	921	991	10.6	15.5
Ti-5Al-2.5Fe	As forged	-	888	939	14.4	33.6
	973K 2h annealed	-	843	901	15.1	37.7
	1003K 2h+H_2	1.24	911	935	17.7	50.3
	1023K 2h+H_2	1.16	955	982	16.4	48.1
	1053K 2h+H_2	0.99	947	1017	13.0	30.9

Note: Alloys dehydrogenated at 948k 8 h after treatment.

The test results clearly indicate that a good combination of strength and plasticity can be obtained when the alloy is hydrogenated at a temperature 0-40K below the H-β transition point and then de-hydrogenated. The old hydrogen treatment process includes a β solid solution treatment. Although hydrogenating in the old process can refine the initial grain structure, it does not refine the β grain sizes; at the same time the process causes the α-phase to form along the grain boundaries.[5] During tension, the slips are hindered by the α-phase along the grain boundaries and stress concentration results. This leads to the fracture of α-phase, which in turn decreases the plasticity of the alloy.

3. Conclusions

The microstructures of the Ti-6Al-4V and Ti-5Al-2.5Fe alloys can be effectively refined. Their strengths and plasticity can be apparently improved when the alloys are hydrogenated at a temperature 0-40K below the H-β transition point, cooled to room temperature, and de-hydrogenated in vacuum (948K).

References

1. Levin, L., Vogt, R. G., Eylon, D., Froes, F. H., In: Luetjering, G., Zwicker, U., Bunk, W. eds., "Titanium, Science and Technology," Vol. 4, Proceedings, 10-14 September 1984, Munich, Oberursel: Deutsche Gesell Metall, 1985: 2107.

2. Kerr, W. R., METALL TRANS., 1985; 16A: 1077.

3. Eylon, D., Yolton, C. F., Froes, F. H., In: Lacombe, P., Tricot, R., Beranger, G. eds., "Titanium Science Technology and Application," Vol. 4, Proceedings, 6-9 June 1988, Cannes, Paris: Les Editions de Physique, 1989: 1523.

4. Stinson, J., Vogt, R. G., Eylon, D., In: White, C. V., Eylon, D., Froes, F. H. eds., "High Integrity Castings," ASM, 1988: 3.

5. Hohn, D. H., Ducheyne, P., J. MATER. SCI., 1991; 26: 328.

Effect of Reinforcement Volume Fraction on Precipitation in SiCp/Al-Matrix Composite

[Article by Lin Junshan [2651 0689 1472], Li Pengxing [2621 7720 5281], and Wu Renjie [0702 0086 3381] of Shanghai Jiaotong University: "Effect of Reinforcement Volume Fraction on the Precipitation Microstructures of SiCp/2024 Duralumin Composites," funded by the Natural Science Foundation of China and the Key State

Laboratory for Metal-Matrix Composites of Shanghai Jiaotong University; MS received 6 Jan 92, revised 29 Jun 92]

[Text] Abstract: The matrix precipitation kinetics of the cast SiCp/2024 metal composite is studied with differential scanning calorimetry (DSC) technique and transmission electron microscope (TEM) analysis. The test results show that the addition of SiC in the matrix 2024 Alloy accelerates the precipitation of the GP zone and the intermediate phase S'(Al$_2$CuMg), and it causes the decrease of the peak temperature of the precipitation reaction. The precipitation enthalpies of the GP zone and the S'-phase are also substantially reduced. TEM analysis shows that the alloy element Mg aggregates along the SiC-Al interfaces, which causes the depletion of all the Mg element near the interfaces. As a result, a precipitation-free zone or precipitation-sparse zone is formed near the interface, and the intermediate phase segregation is reduced.

Compared to continuous fiber-reinforced metal matrix composites (MMCs), the microstructures of non-continuous reinforced MMCs have greater influence on MMC strength and plasticity. Under certain conditions, the contribution of the composite microstructure is the same as, if not greater than, the contribution of the reinforcing phase.[1,2] Past investigations report that the addition of the reinforcing phase to the alloy matrix greatly affects the aging kinetics of MMCs.[3,4] Therefore, it is important to study the precipitation process in the MMC matrix in order to improve the MMC properties.

Using DSC (Differential Scanning Calorimetry) technique, this paper studies the precipitation kinetics in the matrix of the SiC particle reinforced Duralumin 2024. The effect of the reinforced phase volume fraction on the precipitation kinetics is also analyzed. Valuable results are obtained.

1. Experimental Material and Process

The experimental material was made by composite casting. The reinforcing phase was particulate α-SiC of nominal size 14 μm. The matrix was 2024 Duralumin. The volume fractions of SiCp in the matrix were 0 percent, 5 percent, 10 percent, 15 percent, and 20 percent, respectively. The cast ingot was first hot-pressed into a plate of 100 x 50 x 8 mm, then rolled into a sheet of 3.5 mm thickness. The DSC specimens were made according to the volume of the specimen container by linear cutting method. The specimens are small round discs 6.4 mm in diameter and 1.1 mm in thickness.

Heat treatment of the DSC specimens was conducted in a salt bath. For solid solution treatment, the specimens were soaked at 500°C for 1.5 h (hours), then quenched in ice salt water. Before testing, the specimens were soaked in liquid nitrogen to prevent aging. The DSC analysis was conducted with a Perkin Elmer DSC-7 thermal analysis calorimeter. Although the test results were very consistent, each material was still tested at least three more times. The DSC experiment was started at room temperature, and ended at 550°C. The heating rate was 20°C/min. A pure aluminum sheet was used as the reference specimen. The base line method was used to eliminate temperature dependency of the material heat capacity. All the DSC curves were normalized by deducting the SiC mass from the specimen mass so that the contribution of SiC on the heat flow was eliminated.

The microstructure analysis was conducted with a Philips CM-12 TEM. Each TEM specimen was first hand-ground to a thickness of 60 μm, and polished to 15 μm on a Gatan 656/3 precision dimple grinder. Finally, it was thinned again on a Gatan Model 600-TMP ion thinning device.

2. Test Results

Figure 1 shows the DSC curves of the 2024 base metal, 5-vol% SiCp/2024 composite, and 20-vol% SiCp/2024 composite, respectively, in the entire testing temperature range. References 5, 6 report that the curves can be divided into four temperature regions, i.e., the GP (Guiner-Preston) zone formation region, and its solid solution region, as well as the S'-phase (Al$_2$CuMg) formation region, and its solid solution region. In the 40-135°C temperature range, the formation of GP zone makes the system exothermic; in the 135-260°C range, the GP zone forming solid solution with the base metal, endothermic; in the 260-320°C range, the segregation of S' phase, exothermic; above 320°C, endothermic. It can be seen that the addition of the SiCp reinforcing phase only speeds up the same precipitation process. Relative to the base metal curve, the DSC curves of SiCp/2024 composites move horizontally in the low-temperature direction. Furthermore, the addition of SiCp lowers the formation heat of the GP zone, and the segregation heat of the S' phase. Based on the thermal analysis theory,[7] areas under the peaks in Figure 1 represent the enthalpy change ΔH of the respective reactions. The relation between the enthalpy of reaction (heat of reaction) and the volume fraction V_f of the reaction product is expressed in the following equation:[5]

$$\Delta H = (\Delta H_p / MW_p) \times (\rho_p / \rho_s) V_f \qquad (1)$$

where ΔH_p is reaction heat per mol, MW_p is the molecular weight of the precipitation phase, ρ_p is the density of the precipitation phase, and ρ_s is the specimen density. From this equation, it can be seen that the enthalpy of reaction is directly proportional to the volume fraction of the reaction product.

2.1 GP Zone

Figure 2 shows the effect of the SiC volume fraction on the peak temperature T_{GP} of GP zone formation and the enthalpy of formation ΔH_{GP} The formation rate of the GP zone reaches maximum at the peak temperature. The addition of SiC slightly accelerates the formation of the GP zone, as shown by the broken line in Figure 2. However, the formation rate does not further increase with the increase of SiC volume fractions. The "Enthalpy" curve shows the relation of the enthalpy of
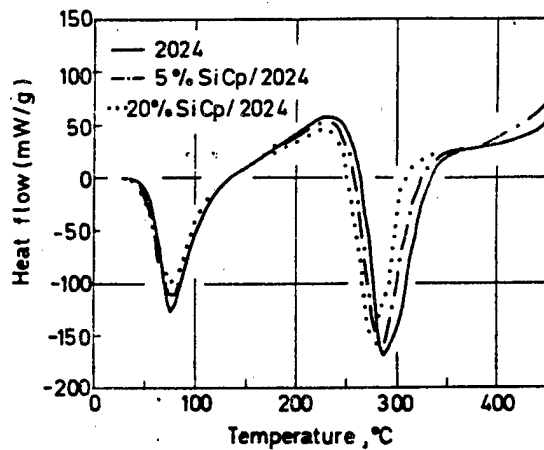
Figure 1. DSC Curves of Precipitation in 0, 5 and 20 vol% SiCp/Al Composites

Figure 2. GP Zone Formation vs SiCp Volume fraction

Figure 3. S' Precipitation vs SiCp Volume Fraction

reaction ΔH_{GP} for the formation of the GP zone and the SiC volume fraction. The addition of a small amount of SiC greatly decreases the ΔH_{GP}. Further addition continuously decreases the ΔH_{GP}, but at a smaller rate. When the composite contains 20-vol% of SiC, its enthalpy of reaction is only 57 percent that of the pure base metal. The calculation from Equation (1) shows that the volume fraction of the GP zone in the base metal of the composite material decreases by 43 percent, which is similar to Papazian's result[6] (40 percent).

The results show that in the 2024 aluminum matrix composite material, the addition of the reinforcing SiCp phase slightly reduces the stability of the base metal solid solution, lowers the peak GP zone formation temperature, and significantly decreases the GP zone formation.

2.2 S'-Phase

SiC affects more the S' phase segregation from the solid solution than the GP zone formation from the solid solution, especially the peak temperature $T_{S'}$. As the straight line in Figure 3 shows, the peak temperature lowers with the increase of S'-phase volume fraction. For this paper, the relation between the peak temperature $T_{S'}$ of the S'-phase segregation and the volume fraction of SiC can be expressed in the following equation:

$$T_{S'} = 288.1 - 61.2 \, V_f.$$

The enthalpy change $\Delta H_{S'}$ of S'-phase segregation is similar to that of the GP zone. Figure 3 shows that the enthalpy decreases exponentially with the increase of volume fraction of SiC. When the SiC volume fraction is 20 percent, $\Delta H_{S'}$ is lowered by about 45 percent, similar to the drop of ΔH_{GP}.

Using the same DSC technique, Papazian[6] studied the precipitation behaviors of the SiC whisker-reinforced
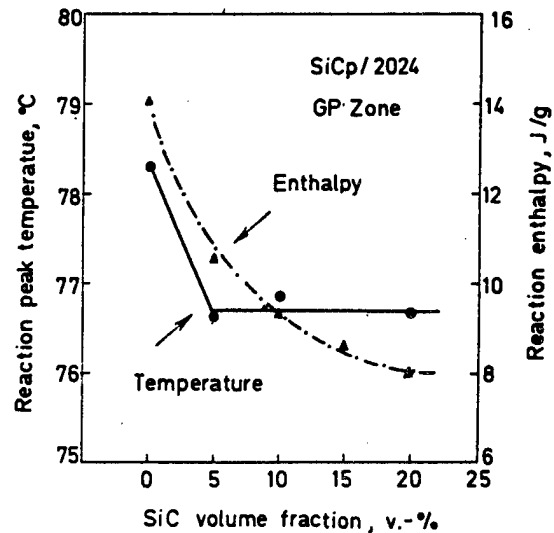
2124, 2219, and 6060 aluminum-matrix composites made by powder metallurgy, as well as the SiC particulate-reinforced 7475 aluminum-matrix composite made by casting. His results conclude: Compared with base metals made by the same process, SiC affects only slightly the GP zone formation peak temperature; it reduces the enthalpy change due to the formation of GP zone; and it also affects only slightly both the peak temperature and enthalpy change of intermediate phase separation. Compared with the results of this paper, it can be seen that the effects of SiC on the composite's microstructure vary with the base metal or the manufacturing method.

3. Discussions

The properties of the constituents in the composite are quite different. They bring about the problem of physical or chemical compatibility, an important research subject. This paper indicates that the effect of the interface on the base metal microstructure should not be neglected, either.

SiCp, when added to the 2024 Duralumin matrix, greatly increases the interface in the material. Moreover, since the thermal expansion coefficients of SiC and Al are greatly different (ratio, 1:10), during manufacturing or heat treating, the dislocation density increases in the matrix, especially along the interfaces, because of the restriction effect along the interfaces.[8] The dislocation density increases with the increase of the volume fraction of SiC.[2] The interfaces and the dislocations form sinks for the residue vacancies produced by quenching. Vacancies have an important impact on the formation of the GP zone.[9] Through different modes, they provide the nonuniform nucleation sites for the formation of the GP zone. The fact that a large quantity of vacancies vanishes in the interfaces reduces the GP zone nucleation rate, and eventually decreases the formation rate of the GP zone. On the other hand, the increase of the dislocation density speeds up the diffusion rate of the alloying elements, and consequently lowers the formation temperature of the GP zone. For the same reason, the segregation temperature of the intermediate phase is also lowered. However, the distances between GP zones (about 10 nm) are much smaller than those between intermediate phases. Hence, the alloy elements require even longer diffusion paths or higher diffusion temperature to form intermediate phases. Therefore, the dislocation effect is much more acute on the segregation temperature of the intermediate phase.

Based on the aforementioned DSC analysis, it can be seen that the segregation enthalpy of intermediate phase S' decreases with the increase of SiC volume fraction. This means that the increase of SiC will decrease the segregation of intermediate phase S'. In the experiment, the composite specimen was heated in a thermal analysis calorimeter to the temperature of the completion of S'-phase segregation (about 310°C) and then immediately quenched in ice water. The specimen was then prepared for TEM microstructure analysis. It is found that the interfaces in the composite are of two types (Types 1 and 2). In Type 1, the precipitation phases exist in the interfaces. Microdiffraction analysis proves that they are Al$_2$CuMg and Al$_2$Cu as shown in Figure 4a [Figure 4 photographs not reproduced]. In Type 2, no precipitation exists on the clear interface, as shown in Figure 4b. In both groups, the precipitation free zones (PFZ) of 0.5-1 μm width in the neighborhood of the interfaces can basically be observed. From the PFZ border in the direction away from the interface, the precipitation phases become larger, and gradually denser—hence the formation of precipitation sparse zones (PSZ). EDAX analysis (electron beam spot diameter: 3.3 nm) shows that there are no alloy elements

aggregated on Type 1 interfaces, and Mg always aggregates on Type 2 interfaces, as shown in Figure 5. Quantitative calculations show that the aggregation quantity is about 8-at%, which is about four times the actual Mg content. The fact that the Mg peak disappears from the spectrograph in a region about 5 nm away from the interface indicates that Mg content in the PFZ is completely consumed. Mg is a very active alloy element, hence it is not surprising that Mg aggregates along the SiC-Al interface as stated in Reference 10 (a paper on the aggregations along the grain boundaries of aluminum alloys). Reference 11 also observes the aggregation phenomenon in the SiC/Al composite. In the interface as shown in Figure 4a, the segregation of the precipitation phase consumes the Mg aggregated along the interface, and consequently, no Mg peak appears in the EDAX analysis. Obviously, the alloy element aggregation on the interface, or the precipitation phase separation from the interface, will deplete the alloy element from the region near the interface and even inside the base metal. Consequently, the segregation of intermediate phases S' is restrained or decreased, and a PFZ or PSZ is formed.
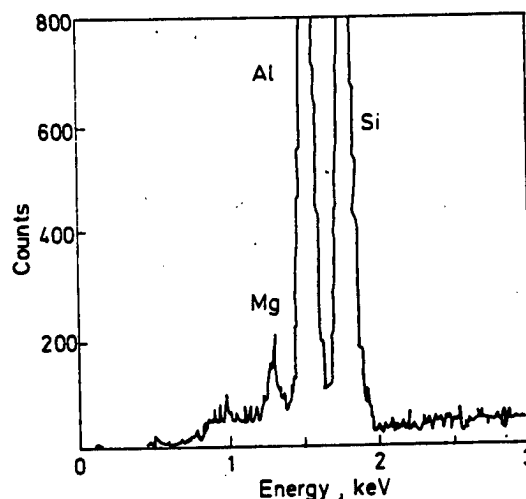

Figure 5. EDAX Spectrum

Based on the above observations, PFZ or PSZ always exists in the base metal in the neighborhood of SiC-Al interfaces. Assuming that SiC is spherical with radius "r," the ratio of volume V_t of PFZ and PSZ to the volume V_m of the base metal can be calculated as follows:

$$V_t/V_m = K[(r + t)^3 - r^3] V_f/r^3 (1 - V_f).$$

In this equation, "t" represents the thickness of PFZ and PSZ zone surrounding SiC, about 1 μm; and "K," the configuration factor of SiC particles. In this paper, SiC powders are mostly in acicular plate shape whose length-to-width ratio is about 0.5, thus the lower limit of "K" has a value of 1.3. From this equation, it can be seen that the density of PFZ or PSZ increases with the increase of volume fraction, and the decrease of the particle size of

SiC. According to the National Standard GB2477-81, W14-SiC powder contains about 72 percent of SiC with a size of 7-14 μm. Substituting these data into the equation, the V_t/V_m value is estimated to be 27-37 percent when the volume fraction of SiC is 20 percent. Since the value is estimated from the lower limit, it is about equivalent to the reduced value (45 percent) of enthalpy change for the S'-phase segregation. Therefore, the formation of PFZ and PSZ is the main cause of the $\Delta H_{S'}$ reduction, and the reduction rate increases with the increase of the SiC volume fraction.

4. Conclusions

The addition of SiCp in the 2024 Duralumin does not change the precipitation process of the base metal. However, the precipitation temperature of the GP zones and especially the segregation temperature of the intermediate phases S' are lowered due to the combined effects of interfaces, dislocations, and the residue vacancies from quenching. The quantity of GP zone formation is also decreased.

In the SiCp/2024 MMC, the fact that the alloying element Mg aggregates in the SiC-Al interfaces causes the decrease of the alloy element in the neighborhood of the interfaces and inside the base metal. Thus, the segregation of the intermediate phase S' is reduced, and PFZ and PSZ are formed in the neighborhood of the interfaces.

References

1. Arsenault, R. J., In: Katawa, K., Umekawa, S., Kobayashi, A. K. eds., Proc. Composite '86: Recent Advances in Japan and the United States, 23-25 June 1986, Tokyo, 1986: 521.

2. Arsenault, R. J., Wang, L., Feng, C. R., ACTA METALL. MATER., 1991; 39: 47.

3. Nieh, T. G., Karlak, R. F., SCR. METALL., 1984; 18: 25.

4. Christman, T., Suresh, S., ACTA METALL., 1988; 36: 1691.

5. DeIasi, R., Adler, P. N., METALL. TRANS., 1977; 8A: 1177.

6. Papazian, J. M., METALL. TRANS., 1988; 19A: 2945.

7. Chen Jinghong, Li Chuanru, "Thermal Analysis and Its Applications," Beijing: Science Press, 1985 [in Chinese].

8. Vogelsang, M., Arsenault, R. J., Fisher, R. M., METALL. TRANS., 1986; 17A: 379.

9. Porter, D. A., Easterling, K. E., "Phase Transformation in Metal and Alloy," Oxford: Alden Press, 1981: 303.

10. Chen, J. M., Sun, T. S., Viswanadham, R. K., Green, J. A. S., METALL. TRANS., 1977; 8A: 1935.

11. Nutt, S. R., Carpenter, R. W., MATER. SCI. ENG., 1985; 75: 169.

Performance, Microstructure of Superhard Si₃N₄ Film by High Power CO₂ Laser CVD

[Article by Feng Zhongchao [7458 6988 3390], Guo Liang [6753 5328], Liang Yong [2733 0516], Han Jian [7281 0256], Hou Wanliang [0230 8001 5328], and Ning Xiaoguang [1337 1420 0342] of the Institute of Metals Research, Chinese Academy of Sciences, Shenyang: "Performance and Structure of Superhard Si₃N₄ Film by Laser CVD," funded by Natural Science Foundation of China; MS received 10 Jun 91, revised 14 Dec 91]

[Text] **Abstract:** The laser CVD method was used to deposit α-Si₃N₄ film on the base metal. The film consists of very fine Si₃N₄ particles which adhere closely to the base metal. The film has super-high hardness, good anti-abrasive, and anti-corrosion properties. The thickness of 5-30 μm can be controlled.

The features of the thin films made by laser chemical vapor deposition (LCVD) are as follows: versatile in composition, able to deposit large range of different materials, low threshold temperatures, high deposition rates, and easy to obtain the other laser produced properties (e.g., laser surface hardening), etc. Internationally, LCVD has been rapidly developed since the 1980's.[1] Deposition research on the Si₃N₄ film on quartz or silica by low power laser has been emphasized[2,3] because the Si₃N₄ film has good mechanical, optical and electrical properties. Since 1987, the authors have studied high-speed, large-area deposition to produce a super-hard film on the metallic base with high power CO₂ laser.[1,4,5] The super-hard film with its high hardness and other special properties (good abrasive resistance, corrosion resistance, oxidation resistance, wave absorbance, etc.) has important value for industrial application and economic significance in technology. This paper presents research on the properties and structure of the Si₃N₄ film deposited on metallic bases by rapid multiple channel lapping deposition (MCLD) method with a high power CO₂ laser.

1. Experiment

The experiment was conducted with locally made LCVD equipment.[5] The base metals were 2Cr13 and 1Cr18Ni8 stainless steels. The reaction gases were SiH₄ and NH₃ as auxiliary gases. These gases reacted chemically under laser and formed Si₃N₄. The deposition rate could reach 15 μm/s which is about 1-2 orders of magnitude higher than previously reported results obtained with low power CO₂ laser deposition of the same film on quartz. The threshold temperature was 640°C, about 200°C

lower than other CVD deposition temperatures. No optical self-limitation phenomenon was observed. The MCLD technique based on the micro-deposition zone technique produced a large-area film (7 cm^2 in this experiment). The best deposition parameters were obtained by the orthogonal intersection design method. The main technical parameters are: laser power density, 200 W/mm^2; laser sweeping speed, 1.5 mm/s; laser spot diameter, 3.0 mm; reactive gas ratio, $NH_3/SiH_4 \approx$ 1,000; deposition chamber pressure, 10 kPa; reactive gas flow speed, 660 cm/s. The micro-topography, chemical composition, and the structure of the deposited film were studied with electronic probe, X-ray diffraction, optical microscope, scanning electron microscope (SEM), transmission electron microscope (TEM), and high resolution electron microscope (HREM). The film properties were measured with profilometer, microhardness tester, scratch abrasive tester, and constant electric potentiometer.

2. Results and Discussion

2.1 Macrotopography and Thickness of Film Layers

The deposited Si_3N_4 film appears to be silvery gray. The film uniformly covers the base metal. No defects such as cracks, pits, or holes are observed. The thickness measurement reveals that the thickness variations of spots are in Gaussian distribution. The maximum thickness reaches about 20 μm. The film obtained with laser scanning MCLD has a uniform thickness with a variation of +/-0.5 μm. The film thickness can be controlled within the range of 5-30 μm.

2.2 Film Layer Composition and Structure

The SEM observation discloses that the film in the greater part of the area is composed of very fine and uniformly distributed grains. The average grain diameter, depending on the deposition technique, is 0.1-3 μm. The film formed under long laser exposure time (e.g., 5 s) or in the lapping zone shows the aggregation of particles, evenly connected plates (Figure 1 [photograph not reproduced]) phenomenon. In the multiple deposition area, the deposition film forms a layered structure. The surface layer is composed of small particles, and the lower layer, of connected plates, as shown in Figure 2 [photograph not reproduced].

Electron probe and Auger energy spectrography show that the ratio of Si atoms to N atoms is about 0.75, which is the chemical composition of Si_3N_4. Its distribution is uniform.[5]

The slow scanning with background suppression method shows the X-ray diffraction patterns. The diffraction patterns of the base metal and the film layer are obtained with TEM. Calculations confirm that the film is α-Si_3N_4. Its lattice parameters are: $a_0 = b_0 = 0.7758$ nm, and $c_0 = 0.5623$ nm.
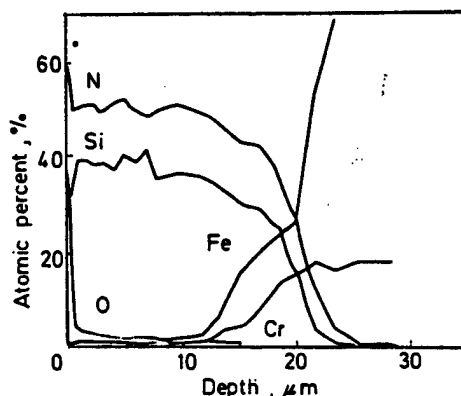

Figure 3. Depth Profile of Elements in Film

2.3 Bonding Zone or Interface of Film and Base Metal

The metallographic study of the cross section of the film formed by MCLD shows that there are two types of bonding: no apparent interface between the film and the base metal as shown in Figure 2a, or a definite interface between them, as shown in Figure 2b. In the former type, a gradual transition zone exists between the film layer and the base metal (Figure 3). The width of the transition zone depends on the deposition condition, about 2-10 μm. This type of metallurgical or diffusion bonding between the film layer and the base metal produces higher bond strengths. The bonding with a definite interface is usually formed by low laser power density deposition or short-period deposition. This interface also provides a good bonding. Figure 4 [photograph not reproduced] displays the HREM image of particles in the Si_3N_4 film layer and the interface, which shows good bonding.

2.4 Microhardness of Film Layer

Figure 5 shows the microhardness data for the film layer measured with a microhardness tester on the metallographic sample of the MCLD film layer cross section. It can be seen that the hardness of the deposition in the horizontal direction is essentially uniform. The hardness of the non-lapping zone is about HK 2200, and that of the lapping zone, HK 2050. No apparent softer spot is observed. In the depth direction, the hardness is also uniform. In the transition zone, the hardness decreases. At the same time, the base metal which is affected by heat also has high hardness (about HK 850-900). This indicated that under certain parameters, the laser depositing the film layer also produces the laser hardening effect.

2.5 Abrasive Resistance and Other Properties of Film Layer

Scratch tests were conducted on specimens of the base metal, the single-channel deposition, the multiple-channel deposition and the lapping zone. The testing conditions were: load, 10.29 N; and number of scratches,
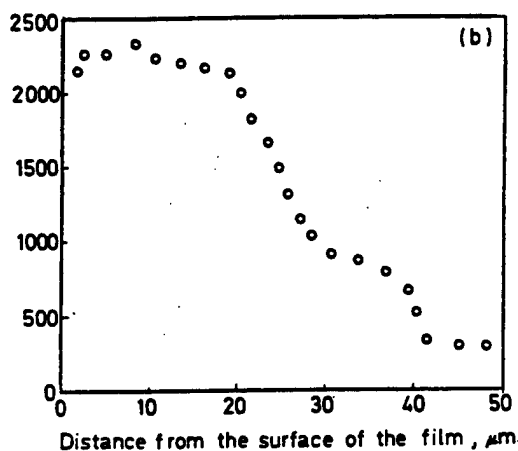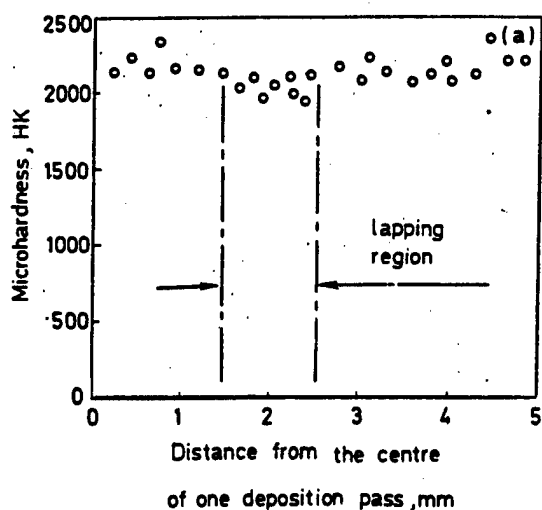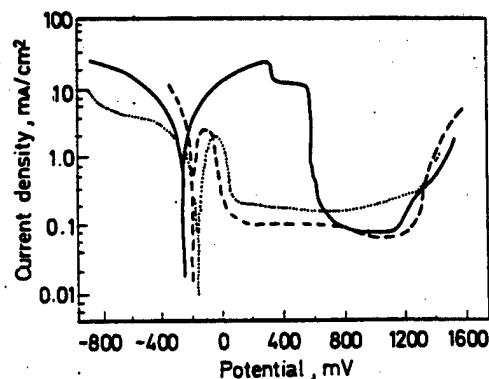
Figure 5. Microhardness Distribution of Film
(a) Cross-section, (b) Along depth

—substrate, —single pass, ···multipass lapping

Figure 6. Polarization Curves of Si$_3$N$_4$ Film and 2Cr13 Substrate in 0.5 mol/L H$_2$SO$_4$ Solution

The scratch test also demonstrates the good bonding strength of the film layer and the base metal. The SEM observation does not reveal any peeling of the scratched film.

The electro-chemical corrosion characteristics of the base metal, the single-channel deposition, and the multiple-channel deposition were tested in 0.5 mol/L H$_2$SO$_4$ corrosion medium with a potentiometer. Figure 6 shows their anodizing curves. It can be seen that the anti-corrosion property of the base metal is greatly improved with the Si$_3$N$_4$ deposition.

3. Conclusion

(1) A high power CO$_2$ laser is used to deposit uniform α-Si$_3$N$_4$ film on the stainless base metal. Most of the film is composed of fine (0.1-3 μm) Si$_3$N$_4$ grains. In some places, the grains aggregate and form connecting plates. It is possible that a composition transition zone which forms a metallurgical or diffusion bonding exists between the film layer and the base metal.

(2) The deposited film has higher hardness, good abrasive resistance, corrosion resistance, and strong bonding force with the base metal. The average hardness of the deposited film is HK 2050-2200. The film's coefficient of abrasive resistance is 7.30-11.73 times that of the base metal.

1,500 times. Table 1 shows that compared with the base metal, the relative abrasive resistance of the single-channel deposition increases by seven times; that of the multiple-channel deposition, 12 times, and that of the lapping zone, 10 times.

Table 1. Comparison of Wear Resistance Among Substrate, Different Pass Deposition and Lapping Region

Description	2Cr13 substrate	Single pass	Two pass	Multi-pass	Lapping region
Scratching trace area, μm²	832	114.0	79.5	70.9	80.2
Relative wear resistance	1	7.30	10.47	11.73	10.38

References

1. Feng Zhongchao, Proceedings of the National Conference for Laser Coating Science and Technology, Shenyang, 1991: 87-95 (in Chinese).

2. Sugimura, A., Fukuda, Y., Hanabusa, M., J. APPL PHYS., 1987; 62: 3222.

3. Pan, E. T-S, Flint, J. H., Adler, D., Haggerty, J. S., J. APPL. PHYS., 1987; 61: 4535.

4. Feng Zhongchao, Liang Yong, Guo Liang, Tong Baiyun, Han Jian, Proceedings of the First National Conference for Laser Processing Technology, Beijing, 1989: 113-117 (in Chinese).

5. Feng Zhongchao, Liang Yong, Guo Liang, Tong Baiyun, Han Jian, In: Huang Liji ed., Thin Films and Beam-Solid Interactions, CMRS Int. 1990 Conf., Vol. 4, Beijing, 18-22 June 1990, Amsterdam: North-Holland, 1991: 459-463.

Microstructure in Laser-Fused High Speed Steel W6Mo5Cr4V2(M2)

[Article by Liu Ning [0491 1337] and Cui Kun [1508 1506] of Huazhong University of Science and Technology, Wuhan, Deng Zonggang [6772 1350 6921] of Hefei University of Technology, and Cheng Benpei [4453 2609 1014] and Kong Jie [1313 2212] of the Institute of Solid State Physics, Chinese Academy of Sciences, Hefei: "Microstructure and Hardness in Laser-Fused M2 High Speed Steel"; MS received 15 Aug 91, revised 11 Dec 91]

[Text] Abstract: The microstructure of laser fused W6Mo5Cr4V2(M2) high speed steel is studied with a scanning electron microscope, a transmission electron microscope, and an X-ray diffractometer. Results show that the microstructure of the deep melted zone reveals a very fine structure identical to that of the chilling zone of ingot solidification. The formation of the narrow chilling zone makes the columnar grains grow into the molten zone. The structure close to the surface of the molten zone contains equiaxed cellular grains. Both the cellular and columnar grains contain martensite and retained austenite. The metal carbides M_6C, Cr_7C_3, and MC distribute along the grain boundaries of the cellular and columnar grains. Due to the existence of martensite, the laser fused structure has a high hardness value of $HV_{0.1}$865-960.

Recently, there have been quite a few reports on the laser treatment of high speed steel.[1-6] Due to the fact that the laser surface melting technique can be used properly to treat the cutting edges of cutting tools,[4] Strutt et al.[4-6] studied the microstructure of the laser fused surface of the M2 high speed steel. They discovered that the laser treatment dissolved the carbide in the M2 high speed steel. After solidification, the microstructure contained austenite and ferrite. The hardness value of the treated steel was only $HV_{0.1}$650-700. No martensite existed in the fused zone. This paper studies the microstructure features of the laser-fused M2 high speed steel, and the reason whether or not martensite exists in the fused zone so that the results can be used for production.

1. Test Material and Method

The starting experiment material was an annealed M2 steel rod of 15 mm in diameter and 4,600 mm in length. Its chemical composition (wt-percent) was: C-0.83, Si-0.25, Mn-0.30, S-0.013, P-0.022, W-6.14, Mo-4.84, Cr-3.98, and V-1.92. The rod was made into test specimens with dimensions 7 x 7 x 30 mm. The specimens were quenched from 1,220°C and tempered three times at 560°C for 1 h. The hardness in the tempered condition was HRC63-65. The specimen surfaces were then phosphated. Laser treatment was conducted in a JCS-033 numerically controlled laser heat treating machine. The machine had a 1.5 kW transverse-mode CO_2 continuous-wave laser. The operating data were: power, 1.2 kW; laser spot diameter, 4 mm, and scanning speed, 10 mm/s.

2. Test Results

Figure 1 [photograph not reproduced] shows the microstructure of the fused zone. It can be seen that the fused zone is approximately divided into three regions. The surface region displays a fine equiaxed cellular structure. The region further inside displays columnar crystals (Figure 1a) which grow in the direction perpendicular to the specimen surface. The distance between the dendrites or the crystal grain diameter is <2 µm. The deep inside region displays a structure similar to that of the chilling region of a solidified ingot (Figure 1b).

TEM (transmission electron microscope) observation of the thin-film specimens shows that the cellular structure on the specimen surface is mainly martensite with a slight amount of carbide distributed along the cellular boundaries (Figure 2a,b [photograph not reproduced]). In addition, some retained δ ferrite exists in the cores of some surface cellular crystals. In the columnar crystal region, the inside structures of the columnar crystals contain martensite and retained austenite (Figure 2c) with carbide distributed along the columnar grain boundaries (Figure 2d).

The distribution of the microhardness values from the surface region to the interior region further proves the aforementioned results. The hardness of the fused zone is $HV_{0.1}$ = 865-960. The hardness on the surface is relatively higher, and gradually decreases until it reaches a minimum. After this point, the hardness increases again. This observation is different for the Strutt's results in which the hardness on the surface was the lowest and gradually increased toward the core.

The sample was ground (peeled) from the surface into different depths and examined with X-rays.[7] The results show that the entire fused zone contains martensite, retained austenite as well as M_6C, Cr_7C_3, and MC type carbides. For comparison, the X-ray measurements of the retained austenite from the peeling tests are also plotted in Figure 3. It can be seen that the fused zone contains about 24.5-31.1 percent of the retained austenite.
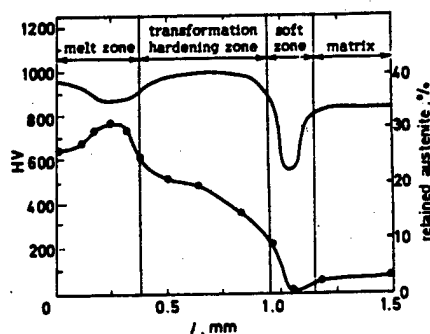
Figure 3. Microhardness and Retained Austenite Content vs Depth Below Surface

HV, - . - retained austenite

TEM EDAX (Electron Diffraction Analysis, X-ray) analysis of the thin-film specimens shows that the columnar grain boundaries are rich in Si. The analysis results show (wt-%): Si-10.61, S-12.74, V-4.18, Cr-8.22, Fe-33.07, W-19.50, and Mo-11.69. In addition, phosphide and sulfide impurities are also observed. The analysis results are (wt-%): P-19.10, S-5.68, V-0.81, Cr-5.20, Fe-61.76, W-1.25, and Mo-6.20.

3. Discussion

The main reason why Strutt's experiment did not obtain martensite while our experiment did is that the two experiments used different laser power rates. This experiment used 9,550 $W/cm^2 \approx 1 \times 10^4$ W/cm^2 while Strutt's experiment used 2.6×10^6 W/cm^2, and obtained a deeper fused zone than our experiment. Furthermore, the surface molten steel temperature of Strutt's experiment was higher due to high laser power, thus, produced higher heat input, reduced the temperature gradient G, and consequently provided a favorable condition to form the coarse columnar crystal structure.[8] When the liquid-solid interface moved toward the surface, the solidification rate R increased[8] and hence increased the tendency to form large columnar crystals as well as shortened the δ-ferrite-liquid reaction time and also increased the diffusion paths for alloy element redistribution. Thus, the peritectic reaction was obstructed and the amount of retained ferrite proportionally increased with the increase of R value. The fact that almost all the δ-ferrite close to the surface region was retained was the main reason that in Strutt's experiment the hardness was low on the surface and it increased toward inner region.

In this experiment, the specimens achieve a martensite structure. Hence, the hardness of the fused zone is higher

and its distribution is different from Strutt's results. From Figure 3, it can be seen that the variation of the hardness values coincides with the variation of the portions of the retained austenite distributions.

From the aforementioned experiment and discussion, it can be seen that the high-power-density laser is not favorable for the completion of the peritectic reaction in the M2 high speed steel. Consequently, the fused zone obtains the structure of δ-ferrite + austenite or even complete δ-ferrite which results in low hardness. A low laser power density can obtain a comparatively shallow fused zone in the M2 high speed steel. This benefits the progress of the peritectic reaction. As a result, the fused zone obtains the martensite structure with higher hardness.

4. Conclusion

(1) The fused zone of the laser melted M2 high speed steel displays a fine cellular crystal structure on the surface, a columnar-crystals structure perpendicular to the surface toward the interior region, and a structure similar to that of the chilled zone of an ingot in the extreme interior region.

(2) The cellular crystals and the columnar crystals consist of martensite and retained austenite, with M_6C, Cr_7C_3, and other MC type carbides distributed along the grain boundaries of the cellular crystals and columnar crystals. Silicon as well as some other phosphide and sulfide exist on the surfaces of the columnar crystals.

(3) The fused zone hardness is comparatively high, $HV_{0.1}865$-960.

References

1. II brheHko B C., MNTOM, 1985, 8:50.

2. II brheHko B C., MNTOM, 1986; 9:11.

3. Kusinski, J., METALL TRANS., 1988; 19A:377.

4. Kin, Y. W., Strutt, P. R., Nowotny, H., METALL TRANS., 1979; 10A-881.

5. Strutt, P. R., Nowotny, H., Tuli, M., Kear, B. H., MATER. SCI. ENG., 1978; 36:217.

6. Strutt, P. R., MATER. SCI. ENG., 1980; 44:239.

7. Liu Ning, Master's Thesis, Hefei University of Technology (in Chinese), 1991.

8. Hu Genxiang, "Jinshuxue [Metallurgy]," Shanghai, Shanghai Science and Technology Press, 1980:174 (in Chinese).

Methods for Investigating Near-Field Power in Ground-Based High Power Laser Weapons Testing

93P60210A Shanghai ZHONGGUO JIGUANG [CHINESE JOURNAL OF LASERS] in Chinese Vol 19 No 12, Dec 92 p 942

[Abstract of paper (#209) by Li Bin [2621 1755] and Du Xiangwan [2629 4382 3834] of the Beijing Institute of Applied Physics and Computational Mathematics presented at the 2nd National Symposium on Laser Propagation in the Atmosphere and Its Engineering Applications, 8-12 Oct 92, UESTC, Chengdu]

[Text] Research on ground-based laser weapons requires specific methods for testing the power of lasers in the atmosphere. Laser beams propagating in the atmosphere are susceptible to scattering by all kinds of particles, with the scattered light intensity determining the laser beam power. Therefore, under certain conditions one can estimate laser power by measuring scattered light power. If one deploys detectors to measure laser scattered light within several kilometers from the light source, the main source of error in laser power estimation arises from uncertainty in laser beam directionality. We propose a multi-detector detection scheme in which a certain number of detectors are deployed around the laser light source at equal intervals from one another. The detectors' angle of elevation and field-of-view angle, as well as the number of detectors, can be adjusted, permitting minimization of power estimation error. We have tried three power estimation methods and have derived three corresponding solid-angle scattering curves, from which we have derived the optimal detection bearing and field-of-view angle, as well as the appropriate number of detectors.

Optical Modulation, Coding of CO_2 Laser Synthetic Aperture Radar

93P60210B Shanghai ZHONGGUO JIGUANG [CHINESE JOURNAL OF LASERS] in Chinese Vol 19 No 12, Dec 92 pp 945-946

[Abstract of paper (#301) by Wang Yongfeng [3769 3057 7685] and Tao Chunkan [7118 4783 1030] of the Military Optics Teaching & Research Section, East China Institute of Technology, presented at the 2nd National Symposium on Laser Propagation in the Atmosphere and Its Engineering Applications, 8-12 Oct 92, UESTC, Chengdu]

[Summary] In order to improve CO_2 laser SAR resolution, one needs to use independent optical systems for radar transmitting and receiving. Under low laser power conditions, we have derived techniques for unit-by-unit coding of the optical pulses to detect the topography of the target object; optical pulse width is 1.367×10^{-7} s and duty factor is 50 percent. We employ germanium as the acousto-optical modulator material producing the coded optical pulses. Modulation frequency of this optical modulator is 7.31×10^8 Hz. The SAR system is carried on board a vehicle [i.e., aircraft or space vehicle].

16-Element Silicon PIN Photodiode Linear Array Developed by Institute 44

93P60213A Beijing WUXIANDIAN [RADIO] in Chinese No 12, Dec 92 p 23

[Article by Chang Ancheng [7022 1344 2052]: "16-Element Silicon PIN Photodiode Linear Array"]

[Summary] MMEI's Institute 44 recently developed the model GT3271Z 16-element silicon PIN photodiode linear array, with the following technical specifications: wavelength response range 0.5-0.9 μm, operating voltage 0 to -15 V, rise time less than 1.2 μs, crossfire factor less than 2 percent, and dark current less than or equal to 3 pA per square mm. This new device has applications in medical equipment, public security border defense monitoring, tracking, guidance, positioning, and other high-tech areas.

Ground Broken for Hebei STN LCD Plant

93P60213B Beijing ZHONGGUO DIANZI BAO [CHINA ELECTRONICS NEWS] in Chinese 19 Mar 93 p 1

[Article by Wei Delu [7614 1795 4389]: "Ground Broken for Jiya Company STN Project"]

[Summary] Groundbreaking for Jiya [0370 7161] Electronics Ltd.'s STN LCD [supertwist-nematic liquid crystal display] project took place in Shijiazhuang, Hebei, on 12 March. This fully automated LCD production line, meeting early nineties international standards, was funded with a gross investment of US$28.95 million and is scheduled to be completed and operational by the end of this year. Annual production capacity will be 383,000 standard displays, with half to be sold abroad.

Theoretical Analysis of RCS From a Finite Frequency Selective Surface

40100074A Chengdu DIANZI KEJI DAXUE XUEBAO [JOURNAL OF UNIVERSITY OF ELECTRONIC SCIENCE & TECHNOLOGY OF CHINA] in Chinese Vol 21 No 6, Dec 92 pp 602-606

[English abstract of article by Deng Shuhui and Ruan Yingzheng of the Dept. of Microwave Eng., UEST of China, Chengdu 610054; MS received 13 Apr 92, revised 20 May 92]

[Text] By using the moment method and the technique of singularity elimination in the field integral, the current distribution, the monostatic and bistatic radar cross section (RCS), and the frequency-selective character of a plate-dipole frequency selective surface (FSS) are analyzed and computed. A general computer program is developed for this kind of applications. The best geometrical sizes of FSS elements at a given central frequency

are obtained. The method, program and results can be directly used in designing low-RCS reflector antennas. By using the symmetric technique, the Toeplitz characteristic technique, the advanced matrix inversion technique, and batch processing in the analysis and computer program, CPU time is substantially saved.

Harmonic Property of Dual-Undulator Free Electron Laser

[English abstract of article by Peng Liangfu, Yang Zhonghai, and Liu Shenggang of the Inst. of High Energy Electronics, UEST of China, Chengdu 610054; MS received 3 May 92]

[Text] The harmonic property of a dual-undulator free electron laser is analyzed by using Madey's theorem. An expression for harmonic spontaneous-emission power density and a small-signal gain formula for this type of undulator free electron laser—as well as coupling coefficients between electrons and radiation field—are derived. From the numerical calculation results it is concluded that the coupling between the electrons and the radiation field can be enhanced by using a dual undulator; the harmonic spontaneous-emission power density and gain hence are increased. Furthermore, under certain conditions, not only odd, but also even harmonic radiation on axis can be obtained.

Programmable Optical Binary Dual-Rail Logic Gate

[English abstract of article by Zhang Zibei and Liu Liren of the Shanghai Institute of Optics and Fine Mechanics, CAS, Shanghai; MS received 8 Nov 91, revised 1 Jul 92]

[Text] Based on dual-rail logic, a cascadable parallel optical binary logic gate is proposed. All 16 binary logic operations can be implemented by this gate, which can be programmed by halfwave phase delay in polarization. The electrooptical effect is proposed to program the logic function in real time and the experimental results are also presented.

Table 1. Sixteen Possible Combinations of Four Instruction Signals S_1-S_4 and the Corresponding Logic Functions of C_1 and C_2

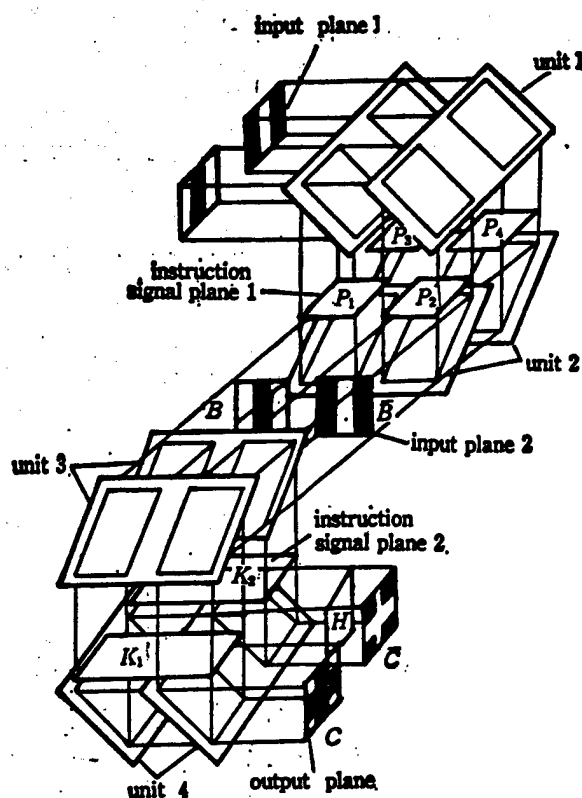| S_4	S_3	S_2	S_1	C_1	C_2
0	0	0	0	F	T
0	0	0	1	AND	NAND
0	0	1	0	A$\bar{\text{B}}$	$\bar{\text{A}}$+B
0	0	1	1	A	$\bar{\text{A}}$

Figure 1. Schematic Diagram of the Optical Binary Dual-Rail Logic System (View A)
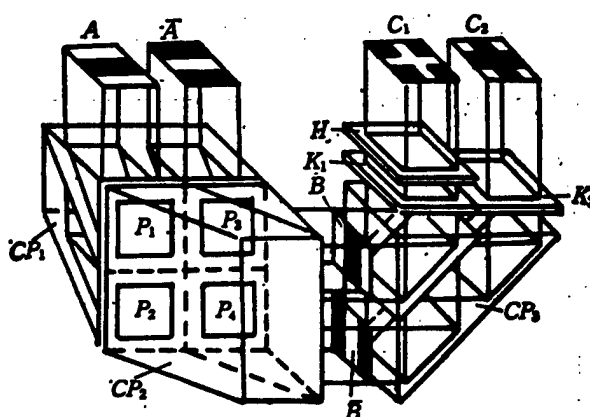

Figure 2. Schematic Diagram of the Optical Binary Dual-Rail Logic System (View B)

CP_{1-3}: composite prisms; P_1-P_4: controllable halfwave plates; K_1-K_2: polarizers; H: halfwave plate

Table 1. Sixteen Possible Combinations of Four Instruction Signals S_1-S_4 and the Corresponding Logic Functions of C_1 and C_2 (Continued)

0	1	0	0	$\overline{A}B$	$A+\overline{B}$
0	1	0	1	B	$\overline{B}$
0	1	1	0	XOR	EQV
0	1	1	1	OR	NOR
1	0	0	0	NOR	OR
1	0	0	1	EQV	XOR
1	0	1	0	$\overline{B}$	B
1	0	1	1	$A+\overline{B}$	$\overline{A}B$
1	1	0	0	$\overline{A}$	A
1	1	0	1	$\overline{A}+B$	$A\overline{B}$
1	1	1	0	NAND	AND
1	1	1	1	T	F

Characteristic Investigation of High-Stability CPM Femtosecond Lasers

[English abstract of article by Wang Shuicai of the Xian Institute of Optics and Fine Mechanics, CAS, Xian; MS received 3 Jan 91, revised 4 Jul 91]

[Text] Using optimization method of dynamic parameters, the operating behavior of a highly stable CPM [colliding-pulse mode locked] femtosecond laser is obtained. The laser output is 43 fs average pulsewidth with a central wavelength at 624 nm, average power of 20 mW, pulsewidth instability of +/-3.3 percent and frequency instability of less than 10^{-6}.

Preparation of CdS Ultrafine Particles, Study of Their Optical Properties

[English abstract of article by Li Shoutian, Zou Bingsuo, Zhang Yan, Xiao Liangzhi, and Li Tiejin of the Department of Chemistry, Jilin University, Changchun 130023, and Zhao Jialong, Zhang Jisen, Huang Shihua, and Yu Jiaqi of Changchun Institute of Physics, CAS, Changchun 130021; MS received 22 Oct 91, revised 6 Mar 92]

[Text] Different sizes in nanometers [6.0-1.0 nm] of CdS ultrafine particles (UFP) are prepared through microemulsion method. Their spectra show that CdS UFPs have a prominent quantum size effect. For the first time, the well-defined structures in CdS UFP emission and excitation spectra at room temperature are found. The emission of surface state is significantly reduced in CdS UFPs modified by surfactant molecules, but that may enhance $X^{(3)}$ of CdS UFPs.

Investigation on p-InGaAs/n-InGaAs MSM Photodetectors

[English abstract of article by Shi Changxin of the Institute of Microelectronic Technology, Shanghai Jiaotong University, Shanghai 200030, A. Mesquida Kuesters, A. Kohl, R. Mueller, and K. Heime of the Institute of Semiconductor Electronics, Technical University of Aachen, Germany; MS received 23 Jun 92, revised 1 Aug 92]

[Text] The $n-In_{0.53}Ga_{0.47}As$ MSM [metal-semiconductor-metal] photodetectors with p-InGaAs Schottky barrier enhancement layer are presented in this paper for the first time. The experimental results indicate that the dark current of devices with a barrier enhancement layer of 20 nm thickness is 3.5×10^{-11} A at 5V bias (30×40 μm^2) and a FWHM of 350 ps (6V) is given by devices with 40 nm-barrier enhancement layer.

Two Domestic Firms, Sumitomo Corp. To Build Optical Fiber Plant

[Unattributed, untitled news brief]

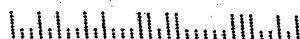[Summary] MPT's Houma Cable Plant and the Taiyuan Optical Fiber Plant have concluded an agreement with Japan's Sumitomo Corp. to construct an optical fiber plant in the Taiyuan High & New Technologies Development Zone. Total investment is 200 million yuan RMB. By 2000, this plant should be able to annually produce 500,000 kilometers of optical fiber. In order to increase annual production of fiber optic cable from the current 5,000 kilometers to 10,000 kilometers, this plant has signed a US$4.45 million contract with a foreign firm for purchase of equipment: two optical fiber jacket bundle machines, two optical fiber color deposition machines, one fiber optic cable cable-forming machine, one protective coating machine, and one ribbon fiber forming machine.

Foreign Broadcast Information Service (FBIS) and Joint Publications Research Service (JPRS) publications contain political, military, economic, environmental, and sociological news, commentary, and other information, as well as scientific and technical data and reports. All information has been obtained from foreign radio and television broadcasts, news agency transmissions, newspapers, books, and periodicals. Items generally are processed from the first or best available sources. It should not be inferred that they have been disseminated only in the medium, in the language, or to the area indicated. Items from foreign language sources are translated; those from English-language sources are transcribed. Except for excluding certain diacritics, FBIS renders personal names and place-names in accordance with the romanization systems approved for U.S. Government publications by the U.S. Board of Geographic Names.

Headlines, editorial reports, and material enclosed in brackets [ ] are supplied by FBIS/JPRS. Processing indicators such as [Text] or [Excerpts] in the first line of each item indicate how the information was processed from the original. Unfamiliar names rendered phonetically are enclosed in parentheses. Words or names preceded by a question mark and enclosed in parentheses were not clear from the original source but have been supplied as appropriate to the context. Other unattributed parenthetical notes within the body of an item originate with the source. Times within items are as given by the source. Passages in boldface or italics are as published.

SUBSCRIPTION/PROCUREMENT INFORMATION

The FBIS DAILY REPORT contains current news and information and is published Monday through Friday in eight volumes: China, East Europe, Central Eurasia, East Asia, Near East & South Asia, Sub-Saharan Africa, Latin America, and West Europe. Supplements to the DAILY REPORTs may also be available periodically and will be distributed to regular DAILY REPORT subscribers. JPRS publications, which include approximately 50 regional, worldwide, and topical reports, generally contain less time-sensitive information and are published periodically.

Current DAILY REPORTs and JPRS publications are listed in *Government Reports Announcements* issued semimonthly by the National Technical Information Service (NTIS), 5285 Port Royal Road, Springfield, Virginia 22161 and the *Monthly Catalog of U.S. Government Publications* issued by the Superintendent of Documents, U.S. Government Printing Office, Washington, D.C. 20402.

The public may subscribe to either hardcover or microfiche versions of the DAILY REPORTs and JPRS publications through NTIS at the above address or by calling (703) 487-4630. Subscription rates will be provided by NTIS upon request. Subscriptions are available outside the United States from NTIS or appointed foreign dealers. New subscribers should expect a 30-day delay in receipt of the first issue.

U.S. Government offices may obtain subscriptions to the DAILY REPORTs or JPRS publications (hardcover or microfiche) at no charge through their sponsoring organizations. For additional information or assistance, call FBIS, (202) 338-6735,or write to P.O. Box 2604, Washington, D.C. 20013. Department of Defense consumers are required to submit requests through appropriate command validation channels to DIA, RTS-2C, Washington, D.C. 20301. (Telephone: (202) 373-3771, Autovon: 243-3771.)

Back issues or single copies of the DAILY REPORTs and JPRS publications are not available. Both the DAILY REPORTs and the JPRS publications are on file for public reference at the Library of Congress and at many Federal Depository Libraries. Reference copies may also be seen at many public and university libraries throughout the United States.